ARTICLE   OPEN

Corrosion-resistant carbide-reinforced martensitic steel by Cu modification

Chen Zhang[1,2], Kenta Yamanaka [ID][2], Huakang Bian [ID][2] and Akihiko Chiba[2]

Carbide-reinforced martensitic steels, known as high-speed steels (HSSs), have been used as tool materials in various industries because of their high hardness and wear resistance. Nonetheless, such steels show severe degradation when used in a corrosive environment because typical Cr_2O_3 films, which generally realise passivity in these alloys, do not often work effectively. Here, we demonstrate that the corrosion resistance of a high-carbon-containing Fe–Cr–W-based alloy in a sulfuric acid solution can be significantly improved by the addition of trace Cu. The enrichment of Cu at the surface of the alloy as corrosion proceeds is key to inhibiting further corrosion. A theoretical model for a micro corrosion cell, which should be applicable to any material employed under the same corrosion conditions in fields such as the chemical and energy industries, was developed to interpret the experimental observations.

INTRODUCTION

The global market for super engineering plastics, particularly polyphenylene sulfide (PPS), has grown in recent years because PPS has a remarkably high temperature resistance, good mechanical strength, and exceptional chemical and solvent resistance in high-temperature environments.[1] One of the most common methods for manufacturing PPS is plastic injection moulding (PIM). However, during this process, the reciprocating screw in the manufacturing apparatus usually suffers from frequent wear loss because the semi-fluid raw materials used for making PPS commonly contain a large amount of glass fibres as a reinforcement. In addition, the mould temperature for the PIM manufacturing of PPS is ~140–300 °C.[2] Therefore, a severe corrosive environment is induced during PIM because PPS is decomposed into SO_2 gas, which then generates an H_2SO_4 corrosive environment via a further series of reactions.[3] Thus, the materials for the screw should be capable of bearing high levels of wear and resisting corrosion during PIM.

Most manufacturers have used traditional stainless steels, such as the SUS300 or SUS400 series, for screw materials. However, the disadvantages of using these materials are evident: in addition to the deterioration of their mechanical properties when used at elevated temperatures,[4] their corrosion resistance under a continuous friction load is still inadequate.

High-speed steel (HSS) is a certain type of alloy (with a C content ranging from 0.6 to 1.3 mass%) that is generally used as a tool material (also in current applications). The outstanding mechanical properties of HSSs at room and elevated temperatures are mainly due to the formation of martensite and numerous carbide precipitates. Powder metallurgy techniques have recently been employed to manufacture HSS with a more uniform distribution of carbide particles in the matrix.[5,6] However, it is inevitable that HSSs will be increasingly susceptible to localised corrosion due to the existence of numerous carbide precipitates.[7–9] Therefore,

there is a great need to improve the alloy design to simultaneously achieve a high hardness and a resistance to corrosion during PIM manufacturing. Moreover, corrosion-resistant HSSs would open further applications in various fields, such as chemicals and energy.

Although a higher Cr content could result in a decrease in strength,[10,11] Cr has been a key corrosion-resisting element in most HSSs. The use of W has been recommended to improve wear resistance, and has been used in the production of W-containing carbides such as WC, which is generically used as a cemented carbide and coating material.[12,13] Although there have already been some studies addressing the microstructures and mechanical properties of the Fe–Cr–W system with the addition of carbon,[14–16] to date there have been no studies addressing its resistance to corrosion in a H_2SO_4 solution. Some simple results obtained for the corrosion mechanism in austenitic steels with a carbon content much lower than that in HSSs would generally differ from those related to carbide-reinforced HSSs in most circumstances. As such, they would likely not be applicable to high-carbon alloys. Nonetheless, Cu is a common alloying element that improves the corrosion resistance of conventional austenitic steels in H_2SO_4 solution because of the higher hydrogen overpotential of Cu[17,18] and/or re-deposition of Cu on the surface.[19,20] However, the effect of Cu addition on the corrosion resistance of high-carbon steels with high carbide contents has not been elucidated.

In this study, we propose a ferrous alloy, produced via Cu alloying, with a high hardness and sufficient corrosion resistance when immersed in an H_2SO_4 solution. Microstructural observations and surface analysis were conducted in detail and the correlation with the corrosion behaviour was examined. It was found that the corrosion of these alloys proceeds starting with the formation of micro corrosion cells; the enrichment of Cu at the surface of the alloy as corrosion proceeds inhibits further

[1]Department of Materials Processing, Graduate School of Engineering, Tohoku University, 6-6-02 Aoba-yama, Aoba-ku, Sendai 980-8579, Japan and [2]Institute for Materials Research, Tohoku University, 2-1-1 Katahira, Aoba-ku, Sendai 980-8577, Japan
Correspondence: Kenta Yamanaka (k_yamanaka@imr.tohoku.ac.jp)

corrosion. A theoretical approach for estimating the localised mixed potential has been proposed to interpret the corrosion mechanisms of these alloys from the viewpoint of the force driving the corrosion reaction.

RESULTS

Alloy design

Several studies have suggested that in austenitic stainless steels, there is a critical Cr content that will provide sufficient corrosion resistance to H_2SO_4 corrosive environments.[21–23] However, because Cr has a strong tendency to form carbides,[24,25] it is generally difficult to achieve high Cr concentrations in the matrix of high-carbon steels. Therefore, it is necessary to make allowances for Cr in high-carbon-content HSSs. Our preliminary experiments confirmed that the corrosion rate of the designed steels decreases with an increase in the Cr content and becomes saturated when the Cr concentration is 13 mass% or higher (Figure S1). Therefore, the Cr content used in the present study was determined to be 16 mass%.

The phase diagram for a Fe–16Cr–3W–1C–xCu system was obtained using a thermodynamic calculation (Thermo-Calc ver. 2017a, via the FE6 Database) as shown in Fig. 1. The austenite (γ), which is required for obtaining the martensitic matrix after quenching, is stable at temperatures above 800 °C for the designed steels. The Cr-enriched $M_{23}C_6$ carbide, which is common in many steels,[24,25] exists in an equilibrium phase. Although WC is not predicted to be present in the current compositions, it was reported that W substitutes for Cr in the $M_{23}C_6$ carbide, as well as the coarsening rate of the $M_{23}C_6$ carbide particles at high temperatures, decreases as the diffusion of W becomes a rate-controlling process.[26–28] Furthermore, W substitution has been known to increase the hardness of the $(Cr, Fe)_{23}C_6$ carbide significantly.[29] Therefore, a small amount of W (3 mass%) was added to the alloys used in the present study to realise a smaller carbide particle size and higher hardness. The thermodynamic calculations also indicate the precipitation of pure Cu at relatively low temperatures. To build the experimental and control groups with which to discuss the effect of Cu addition to the Fe–Cr–W–C alloy, Fe–16Cr–3W–1C without and with 2 mass% Cu (hereafter

denoted as Cu-free and Cu-added alloys, respectively) were designed (see the dashes in Fig. 1). To obtain the martensitic matrix and ensure the dissolution of Cu into the matrix phase, the alloy samples were heat-treated at 1000 °C for 2 h, followed by water quenching.

Microstructures

Figure 2 shows the (a, d) image quality (IQ) maps, (b, e) inverse pole figure (IPF) maps, and (c, f) phase maps of the Cu-added alloy in the (a–c) as-cast and (d–f) quenched states, as obtained by electron backscatter diffraction (EBSD) measurements. The as-cast specimen had a very coarse dendritic microstructure with grain sizes of several hundred micrometres. In contrast, the microstructure of the quenched specimen (Fig. 2d) was much finer. The phase maps indicate that the matrix of the as-cast specimen consisted mainly of austenite with a face-centred cubic (fcc) structure, with most parts of the microstructure being replaced by the body-centred cubic (bcc) phase after heat treatment. This phase transformation was also identified by X-ray diffraction measurements (Figure S2). Furthermore, as shown in Figure S3, the crystallographic orientations of the matrix satisfied the Kurdjumov–Sachs (K–S) orientation relationship ($(111)_{fcc}$// $(011)_{bcc}$, $[\bar{1}01]_{fcc}$//$[\bar{1}\bar{1}1]_{bcc}$), which is a characteristic commonly observed for lath martensite in steels,[30] while numerous dislocations were observed in the matrix phase (Figure S4). These results suggested the occurrence of a martensitic transformation upon quenching. Similar behaviour was also observed for the Cu-free alloy.

Figure 3 shows backscattered electron (BSE) images for the Cu-free and Cu-added alloys in the as-cast and quenched states, respectively. The as-cast specimens have precipitates exclusively at the grain boundaries (Fig. 3a, b). In contrast, two kinds of precipitates with different scales were observed in the matrices of both alloys after heat treatment, as shown in Fig. 3c, d. Notably, the quenched specimens exhibited numerous nano-sized precipitate particles with diameters of 50–200 nm in both alloys, while such fine precipitates were not observed in the as-cast microstructures of both alloys. Hereafter, the observed coarse and fine precipitates are referred to as primary and secondary precipitates, respectively.

Figure 4 shows the (a) high-angle annular dark field (HAADF) scanning transmission electron microscopy (STEM) image and the (b–f) corresponding energy-dispersive spectroscopy (EDS) elemental maps for the quenched Cu-added sample. Higher Cr, W, and C contents were identified within both the primary and the secondary precipitates, while Fe and Cu were depleted. EDS point analysis suggested that the matrix phase contained ~12 mass% of Cr and 3 mass% of Cu, with no significant compositional difference between the two kinds of precipitates (Table 1).

Figure 5 shows high-resolution HAADF-STEM images and the corresponding selected area electron diffraction (SAED) patterns for the (a) primary and (b) secondary precipitates, respectively, in the quenched Cu-added sample. From the SAED pattern, the primary precipitate could be identified as $M_{23}C_6$ carbide with a zone axis in the [001] direction. The secondary precipitate was also identified as being the same $M_{23}C_6$ carbide. Therefore, both the primary and secondary precipitates observed in the alloys consisted of $M_{23}C_6$ carbide. According to the calculated phase diagram (Fig. 1), $M_{23}C_6$ carbide exists as an equilibrium phase with a wide range of temperatures, and no other carbide is predicted to form in the current composition. The primary $M_{23}C_6$ carbide, which had a lamellar morphology, was likely produced via a eutectic transformation during solidification and remained after heat treatment. It should be noted that Cu was preferentially distributed to the matrix.
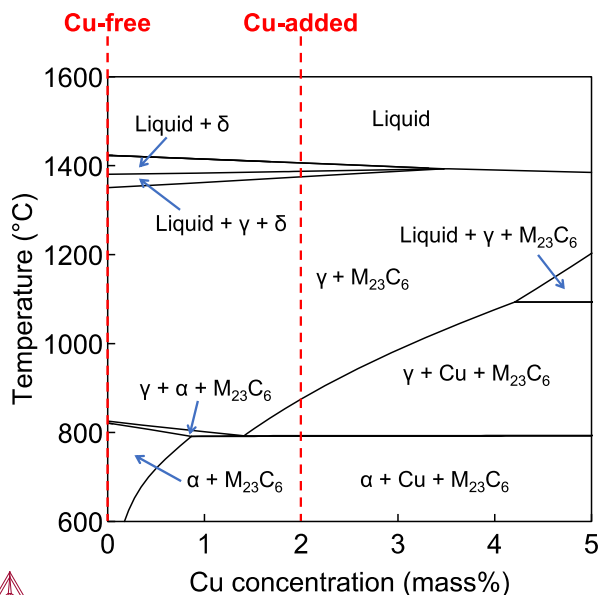

Cu-free   **Cu-added**

Fig. 1 Vertical section of phase diagram calculated for Fe–16Cr–3W–1C–xCu (mass%) system. The dashed lines indicate the chemical compositions of the Cu-free and Cu-added alloys
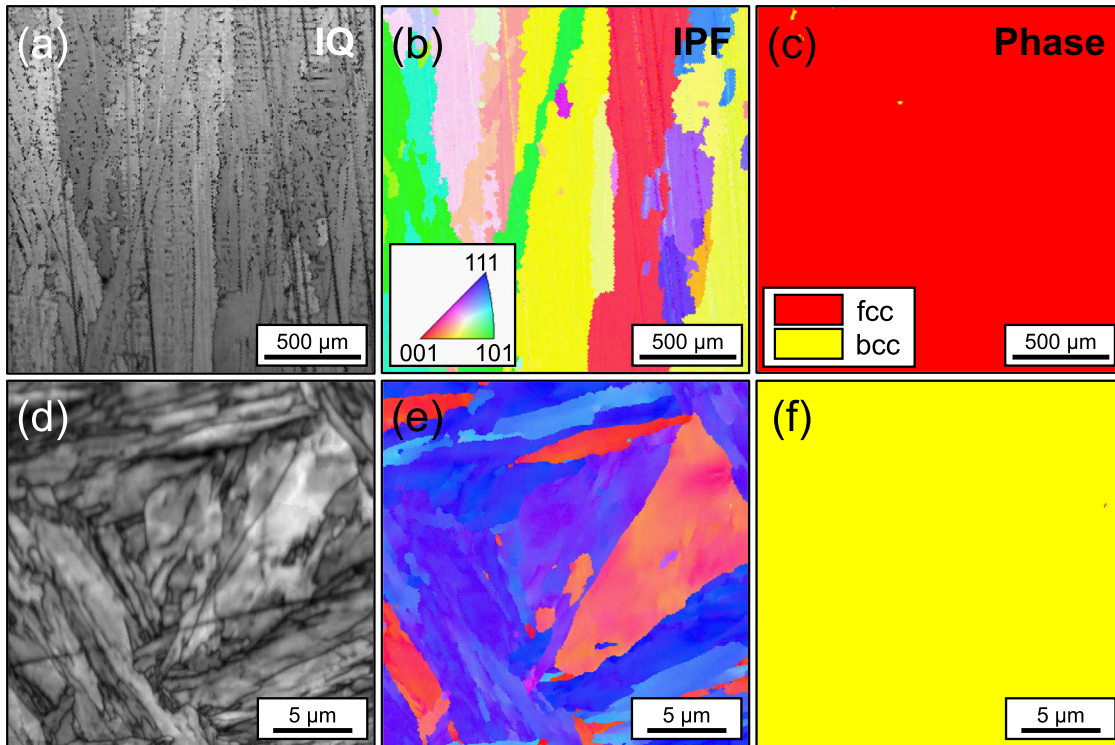
Fig. 2 **a**, **d** Image quality (IQ) maps, **b**, **e** inverse pole figure (IPF) maps, and **c**, **f** phase maps for specimens of **a–c** as-cast and **d–f** quenched Cu-added alloys
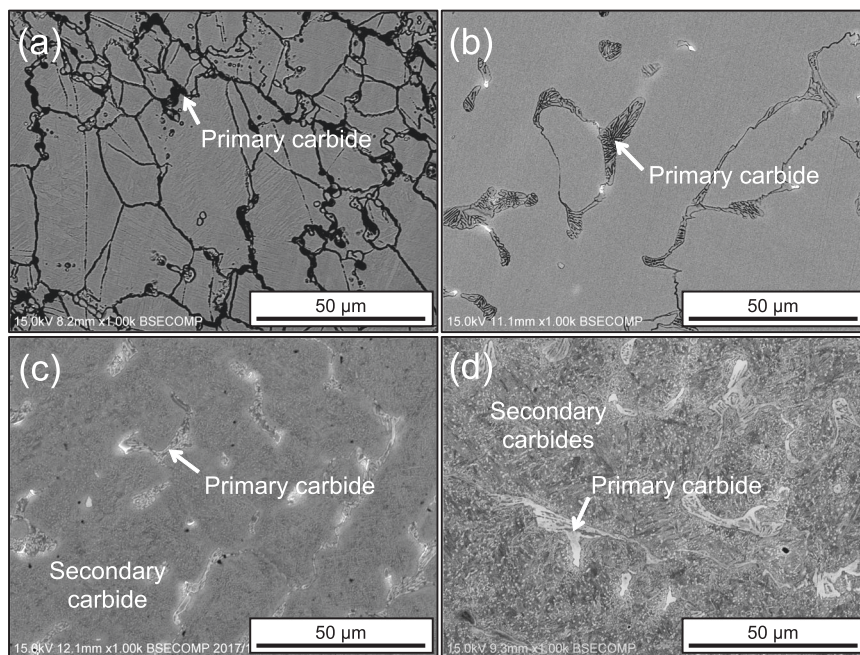

Fig. 3 Backscattered electron (BSE) images for the **a**, **b** as-cast and **c**, **d** quenched **a**, **c** Cu-free and **b**, **d** Cu-added alloy specimens

Vickers hardness

Figure 6 shows the Vickers hardness values for the as-cast and quenched samples of each alloy. The Vickers hardness for the former was 360 and 322 HV for the Cu-free and Cu-added alloys, respectively. Both alloys exhibited a considerable increase in hardness after quenching due to the formation of significantly finer martensitic microstructures with numerous carbide precipitates. As a result, very high Vickers hardness values, i.e. exceeding 700 HV were achieved in the quenched samples for both compositions. The results of a t-test suggest that a slight decrease in the hardness occurred when a small amount of Cu was added to both the as-cast and quenched specimens.
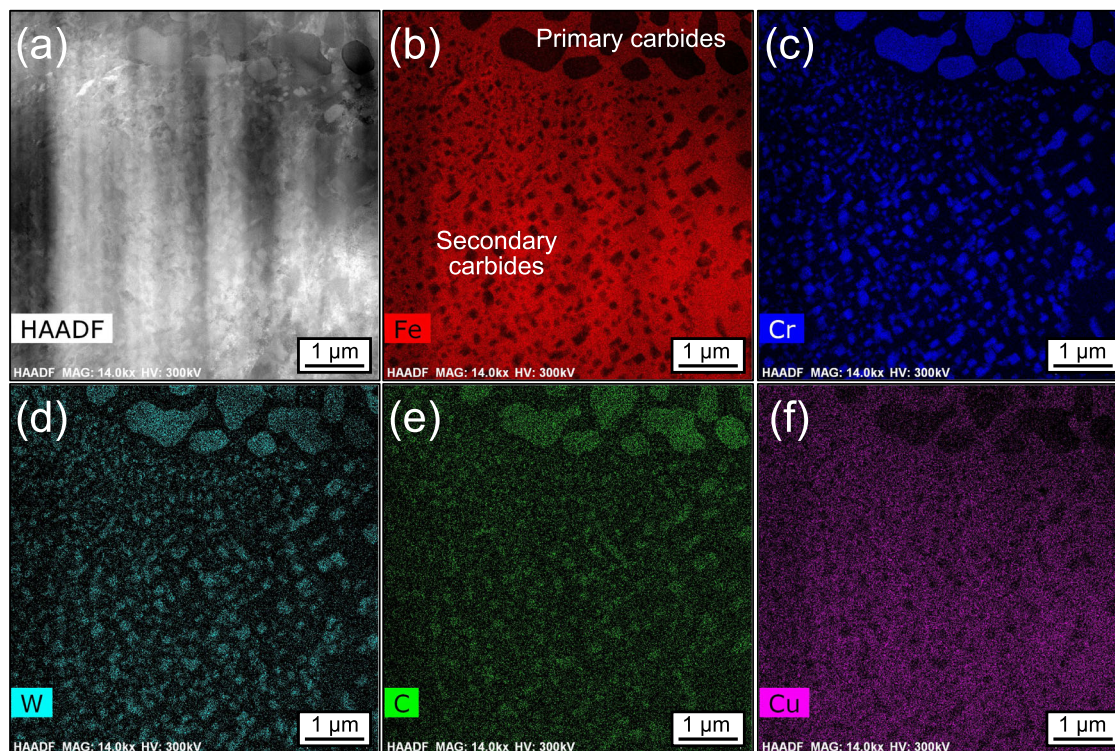
Fig. 4 **a** High-angle annular dark field-scanning transmission electron microscopy (HAADF-STEM) image and **b–f** corresponding energy-dispersive spectroscopy (EDS) elemental distribution maps of the quenched Cu-added sample

Table 1. Quantitative STEM-EDS point analysis results (average $\pm 3\sigma$) for matrix and carbides in quenched Cu-added alloy (mass%)

	Fe	Cr	W	Cu	C
Matrix	82.87 ± 7.68	12.36 ± 1.32	1.89 ± 0.78	2.88 ± 0.49	–
Primary carbide	34.20 ± 3.54	51.75 ± 5.09	8.28 ± 2.95	0.48 ± 0.29	5.29 ± 1.07
Secondary carbide	37.14 ± 3.67	45.03 ± 4.36	11.44 ± 3.77	1.63 ± 0.42	4.76 ± 0.86

Corrosion performance

Immersion tests were conducted to evaluate the corrosion properties of the as-cast and quenched samples. During immersion in a 1 N sulfuric acid solution, hydrogen bubbles (H_2) were generated from the surface of the Cu-free alloy specimen only after the first measurement (within 1 h). As the time progressed, the sulfuric acid solution turned light cyan and the surface of the Cu-free sample blackened. In contrast, negligible bubbling was observed for the Cu-added alloy in the first 2 h. After 7 h of corrosion, the surface of the sample turned brown to some extent.

Plots of weight loss as a function of the immersion time for the as-cast and quenched specimens were calculated and are shown in Fig. 7a. Overall, the weight loss of all the specimens increased with the immersion time. The value for the as-cast Cu-added alloy specimen was lower than that for the Cu-free counterpart, with the difference between them increasing significantly with the immersion time. The quenched Cu-added samples exhibit an almost constant weight loss, similar to those in the as-cast state. However, the Cu-free counterpart showed an accelerated increase in weight loss with immersion time. Consequently, there was a more significant difference between the alloys in the quenched state after 7 h of immersion.

The corrosion rates, which were converted from the weight loss plots, are shown in Fig. 7b as a function of the immersion time. Both in the as-cast and quenched states, the corrosion rates of the

Cu-added alloy samples were more than one order lower than those of their Cu-free counterparts. When the corrosion duration exceeded 4 h, the distances between any two curves become almost invariant on a logarithmic scale. Therefore, the corrosion resistances of the Cu-added specimens in both the as-cast and quenched states were higher than those of the Cu-free specimens, particularly in the case of longer immersion times. The corrosion resistances of both the Cu-free and Cu-added samples decreased after water quenching. However, this deterioration trend in the Cu-added specimens was negligibly small when compared to those for the Cu-free specimens.

Based on the results of the immersion experiments, we can conclude that the addition of Cu to Fe–Cr–W–C alloys not only significantly improves their corrosion resistance in a dilute H_2SO_4 solution, but also inhibits the corrosion resistance deterioration caused by the water quenching treatment.

Corrosion microstructures

Figure 8 shows scanning electron microscopy (SEM) images corresponding to the corroded microstructures of the (a, c) Cu-free and (b, d) Cu-added alloy samples in the (a, b) as-cast and (c, d) quenched states. Although crevices around the carbide precipitates were observed, particularly in the as-cast samples, a more severe dissolution occurred in the matrix phase. Notably, the martensitic matrix in the quenched Cu-free specimens reacted
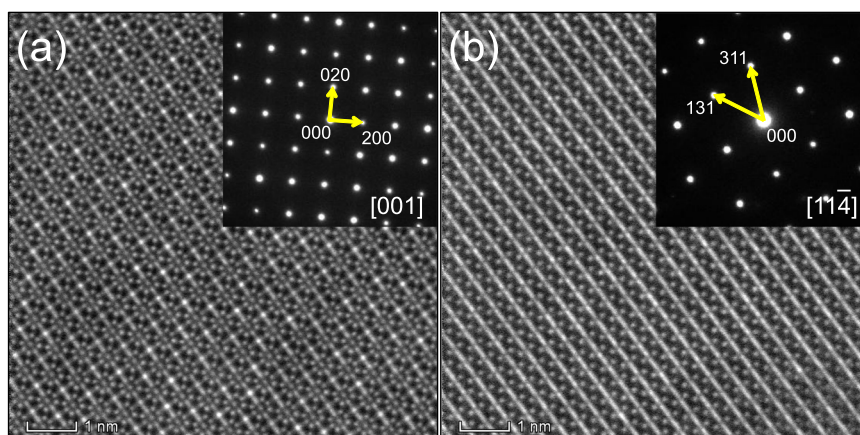
Fig. 5 High-resolution high-angle annular dark field-scanning transmission electron microscopy (HAADF-STEM) images and corresponding selected area electron diffraction (SAED) patterns for **a** primary and **b** secondary carbides in quenched Cu-added specimen
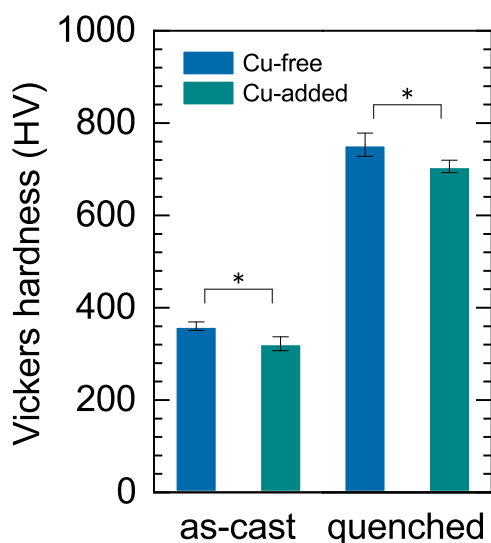

Fig. 6 Vickers hardness of Cu-free and Cu-added alloy specimens before and after water quenching. The asterisks indicate significant differences between the indicated groups; *$p < 0.05$

completely with the acid solution, resulting in the formation of primary carbides with a net-like morphology. In contrast, even in the quenched state, the matrix of the Cu-added sample was considerably less affected by the H_2SO_4 solution and essentially survived the immersion test. After the 7-h immersion tests, the maximum surface roughness (Rz) of the quenched Cu-free sample was approximately 45 µm, which is more than double those of the other samples. These results indicate that corrosion occurred mainly in the alloy matrix, resulting in a significant surface roughness.

Preferential dissolution

The preferential dissolutions of the alloying elements during the immersion tests were investigated based on a solution analysis. The ionic concentrations in the solution of the as-cast samples after the tests following 7 h of immersion are summarised in Fig. 9a. The ionic concentration of Fe in the solution was higher than those of other elements in the H_2SO_4 solutions used for the immersion tests of both the Cu-free and Cu-added specimens. Nonetheless, the addition of 2 mass% Cu to the alloys significantly inhibited the dissolution of metallic elements into the solutions. A low level of Cu dissolution was also detected in the Cu-added alloy.

Figure 9b shows the concentration fractions for the metallic elements (Fe, Cr, W, and Cu) in each solution, as calculated from Fig. 9a. The alloy matrix compositions, denoted by dashes, can be regarded as being the expected values under the assumption that no preferential dissolution occurs. Therefore, the differences in the values of the concentration fractions in the solution and the composition of the corrected matrix indicate the dissolution preferences of the alloying elements. To acquire more precise matrix compositions for each alloy, the corrected values were calculated using the maximum posteriori Bayesian inference method,[31] which considers the nominal composition as priori and the 20 different measurements of the alloy matrix of the as-cast samples as the posteriori observations. The latent dissolution tendency for each element can be obtained using the following criterion: if the concentration fraction in the solution for a specific element is higher than its alloy content the element is dissolved preferentially during corrosion, and vice versa. The results indicate that in the Cu-free specimen, W has limited dissolution while Cr exhibits proportional dissolution. In this condition, a Cr-enriched protective surface is less likely to form. In contrast, for the Cu-added specimen, most metallic elements (Cr, W, Cu) exhibit limited dissolution.

Surface analysis

Figure 10 shows the results of the X-ray photoelectron spectroscopy (XPS) survey analyses for the as-cast and quenched (a) Cu-free and (b) Cu-added samples before and after the immersion tests, respectively. There are major peaks corresponding to the metals, i.e. Fe 2p, Cr 2p, W 4f, O 1s, and Cu 2p (Cu-added alloy only). Both the as-cast and quenched Cu-added samples after immersion exhibit high-intensity Cu peaks.

The narrow scan profiles of the Fe 2p, Cr 2p, and W 4f peaks of the quenched specimens after immersion for 1 h are shown in Fig. 11a–f; the as-cast specimens exhibit no differences from the quenched ones. In each narrow scan profile for a metallic element, envelope peaks are deconvoluted into the peaks of the metallic and oxidation states, as denoted by the blue and magenta lines, respectively. Fe (Fig. 11a, d) and Cr (Fig. 11b, e) exist simultaneously as metals and oxides in the Cu-free and Cu-added specimens. However, the peaks of the metallic state in the Cu-added specimen are significantly stronger than those in the Cu-free one. W exists as both a metal and W^{6+} for both alloys and there is no significant difference in the narrow scans for W between the Cu-free and Cu-added specimens in Fig. 11c, f. The profile of Cu after the immersion (Fig. 11g) shows that most Cu exists in a metallic state on the surface of the Cu-added specimen after corrosion.
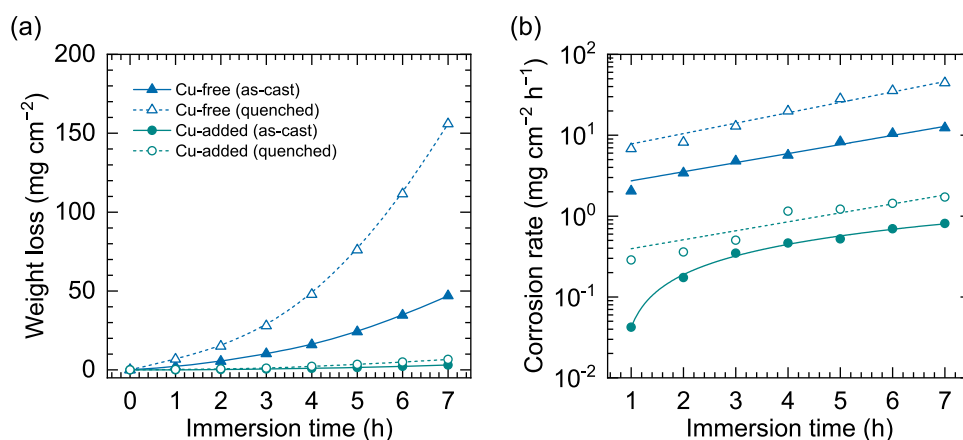
Fig. 7 **a** Weight loss and **b** corrosion rate as functions of immersion time for as-cast and quenched Cu-free and Cu-added alloy specimens
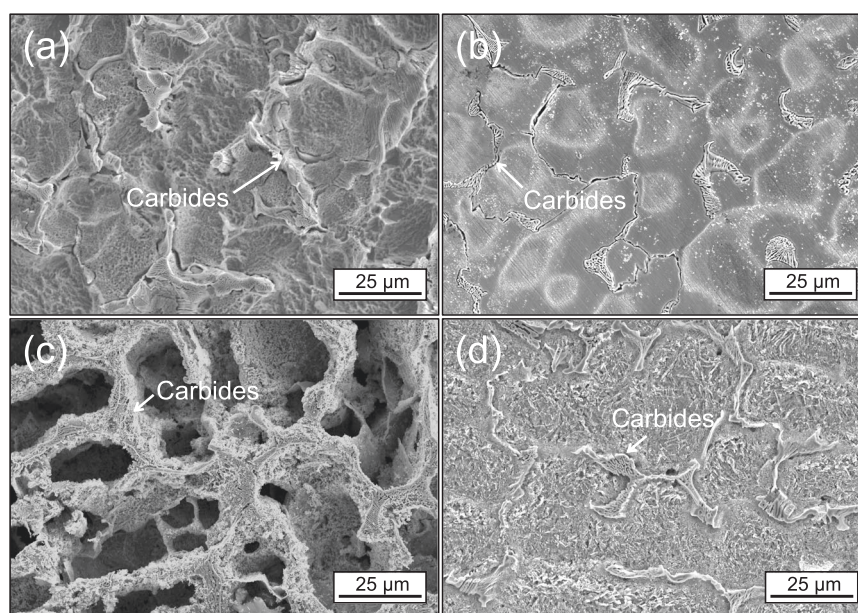

Fig. 8 Scanning electron microscopy (SEM) images for **a**, **b** as-cast and **c**, **d** quenched specimens of **a**, **c** Cu-free and **b**, **d** Cu-added alloys after 7 h of corrosion in 1 N H_2SO_4 at room temperature

The depth-wise profiles of the elemental distributions for the as-cast and quenched Cu-free and Cu-added specimens after 1 h of immersion were determined from the XPS data and are shown in Fig. 12. The oxygen concentrations after immersion were ~75 at.% and 60 at.% on the outermost surfaces of the Cu-free and Cu-added samples; thus, they were higher than the concentrations measured before the immersion tests. Notably, the enrichment of Cr in the outermost surface oxide was not observed in either alloy after immersion. This indicates that the Cr_2O_3 layer, which generally acts as a passive film in corrosion-resistant steels, does not contribute to the corrosion resistance of these alloys, although the Cr concentration of the matrix was as high as 12 mass% (Table 1). Instead, a W-enriched surface appeared in the as-cast Cu-free specimen (Fig. 12a) after the immersion possibly as a result of preferential dissolution (Fig. 9b). The same phenomenon was not observed in the quenched Cu-free sample (Fig. 12c), possibly because more severe dissolution of the matrix phase occurred in the quenched state (Fig. 8c). In contrast, Cu was concentrated on the surfaces of both the as-cast and quenched Cu-added samples after the immersion, as shown in Fig. 12b, d. This indicates that the

enrichment of Cu at the surface of the alloy as corrosion proceeds is key to inhibiting further corrosion.

Furthermore, the depths of the corrosion-induced surfaces increased in the quenched Cu-free and Cu-added samples after immersion (Fig. 12c, d), as shown by the vertical dashes determined by the Fe distributions. For the quenched Cu-added samples, the depth (~200 nm) of the corroded surface increased only 2–3 times compared to that of the as-cast one; however, this is not less than 10 when compared to the depths of the corrosion-induced surfaces in the Cu-free group (Fig. 12a, c).

DISCUSSION

Our experimental results showed that, despite the high Cr content (16 mass%), the Cu-free alloys have a marked susceptibility to corrosion in a dilute sulfuric acid solution. Microstructural observations and surface analysis of the Cu-free sample revealed that the corrosion was more severe within the matrix phase, resulting in considerable active dissolution. This is reasonable because the Cr concentration, which is as high as those (e.g. higher than 18 mass% for SUS304) of stainless steels with good

corrosion resistance to sulfuric acid solutions, cannot be achieved in the matrix of designed alloys with large amounts of carbides. Thermodynamic calculations suggested that the equilibrium Cr content in the alloy matrix (austenite) at the annealing temperature (1000 °C) of the present steels is as low as 10 mass % (Figure S5), which is consistent with the experimental results (Table 2).

On the other hand, Kelvin force microscopy (KFM) observations revealed a potential difference between the carbide precipitates and the surrounding matrix (Figure S6). Such a difference must contribute to the corrosion reaction and this may appear as micro-galvanic corrosion[32] at the carbide–matrix interfaces. However, Cr depletion around the carbide particles, which act as preferential

sites of localised corrosion attacks, was not evident in the current steels (Figure S7). Instead, in the as-cast samples, corrosion was initiated not only at grain boundaries with primary carbides but, more significantly, in a matrix with no carbide precipitates (Figure S8). Therefore, we concluded that the micro corrosion cell mechanism,[33,34] which also consists of microscopically separated anodes and cathodes, and therefore causes corrosion at the grain interiors, plays a dominant role in the corrosion of the studied alloys.

The micro corrosion cell model is schematically shown in Fig. 13. The high Cr- and W-containing carbides served as cathodes and the alloy matrix was the anode. The difference in the electrochemical potential between the anode and cathode drove the directional flow of electrons according to the blue arrows denoted in Fig. 13. The cathodic reaction began at the carbides, generating hydrogen gas. It is clear that a difference in the electrochemical potential between the anode and cathode caused the local breakdown of the passive film on the surface of the sample and thus made it impossible for a stable and continuous protective structure to form there. The typical Evans diagram for steel in a non-oxidising acid suggests that the corrosion reaction in the Cu-free Fe–Cr–W–C system is subject mainly to anodic control.[35,36] The mechanisms for anodic polarisation can be subdivided further into three types: activation, concentration, and resistance polarisation. The first two are strongly related to the diffusion behaviours of metallic cations in solution, which can be ignored if we assume an ideal solution (an infinite solution environment) with a more than sufficient diffusion rate. This assumption is reasonable in the present immersion tests in a dilute H_2SO_4 solution and in our practical problem with PIM manufacturing, because the material used for a screw is always fixed while corrosive substances are generated and stirred continuously. Therefore, more attention needs to be given to the third type, resistance polarisation, which is caused by the formation of some chemical substances in the anode.

Here, a theoretical approach is employed to interpret the two different corrosion mechanisms for the Cu-free and Cu-added alloys from the viewpoint of the driving force leading to the corrosion reaction. All our inferences are made under the ideal solution assumption.

Given that surface analysis revealed that the alloying elements in the studied steels are selectively dissolved during the immersion tests, the overall corrosion process can be described as a dealloying process. Therefore, in accordance with the results of a previous study,[37] we employed the mixed potential theory[35] to interpret the corrosion behaviour of the current alloys. Although the previous study focused on binary systems, the
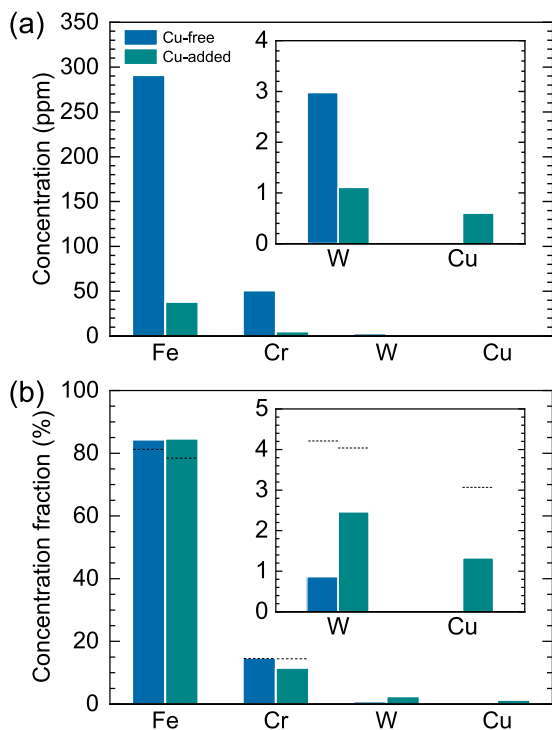

Fig. 9 a Absolute concentrations and b concentration fractions of all metallic elements in H_2SO_4 solution after 7-h immersion test for as-cast Cu-free and Cu-added samples at room temperature. The alloy matrix compositions, which were determined for each sample before the immersion test, are denoted by dashed lines
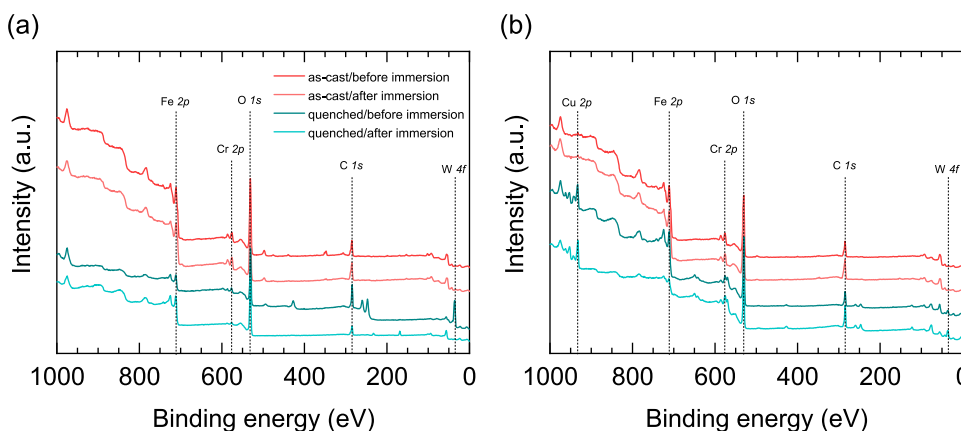

Fig. 10 Survey scans for as-cast and quenched a Cu-free and b Cu-added specimens before and after immersion tests in 1 N H_2SO_4 solution for 1 h at room temperature
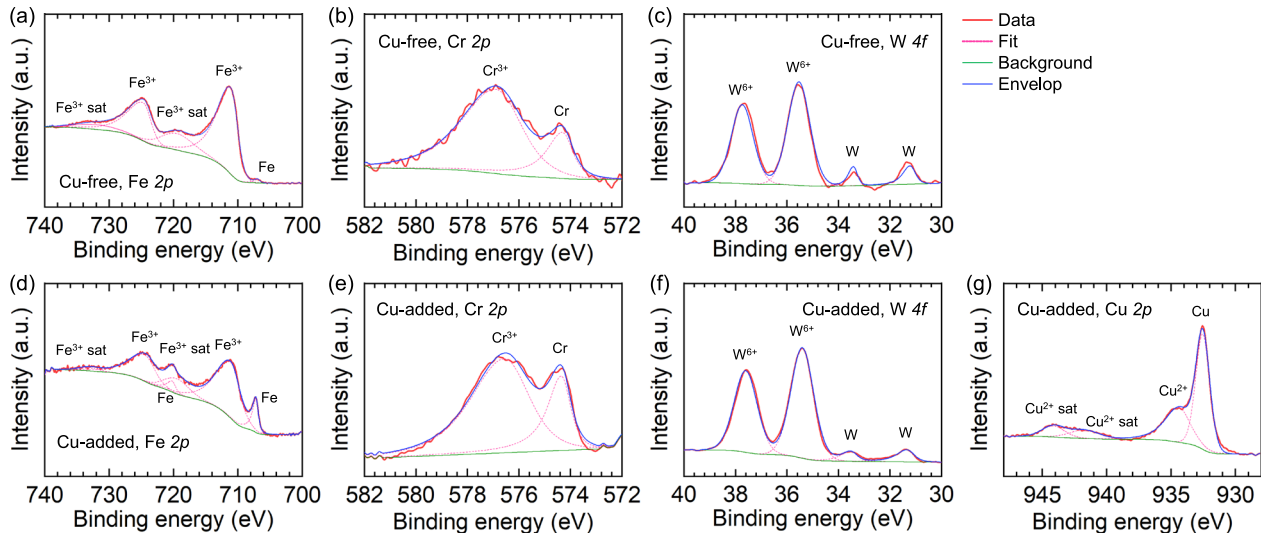
Fig. 11 Narrow scans of **a**, **d** Fe 2p, **b**, **e** Cr 2p, **c**, **f** W 4f, and **g** Cu 2p for quenched **a**–**c** Cu-free and **d**–**g** Cu-added specimens after 1 h of immersion in 1 N H_2SO_4 solution at ambient temperature
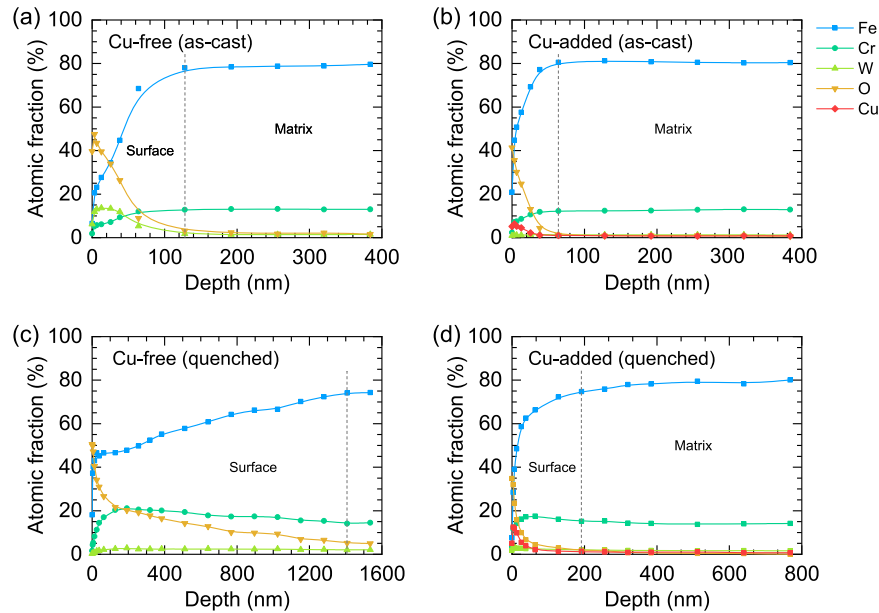

Fig. 12 Depth-wise atomic elemental fractions of Fe, Cr, W, Cu, and O in **a**, **b** as-cast and **c**, **d** quenched **a**, **c** Cu-free and **b**, **d** Cu-added specimens after 1 h of immersion in 1 N H_2SO_4 acid solution at room temperature

potential for the anode $(\widehat{\mu_{mix,A}})$ can be extended to multi-component systems, as expressed by the following equation:

$$\widehat{\mu_{mix,A}} = \sum_i w_i \mu_i \tag{1}$$

where i denotes the index for each content. The parameter $\mathbf{w} = (w_1, w_2, \ldots, w_i)$ will always satisfy the following condition:

$$\mathbf{w} \in \{\mathbf{w} | w_1, \ldots, w_i \geqslant 0, w_1 + \cdots + w_i = 1\} \tag{2}$$

Therefore, the parameter $\mathbf{w}$ can be seen as a multi-dimensional variable that conforms to the the Dirichlet distribution.[38] For any specified content, considering the right-hand limit: $w_i \to 1^-$, the relationship, $\lim_{w_i \to 1^-} \sum w_i \mu_i = \mu_i$, is invariably established and there is an implied condition, $\sum w_i = 1$, in the Dirichlet distribution. Consequently, it is acceptable to consider the atomic fraction as w_i, for each item of content individually. Therefore, in Eq. (1), we

only need to make another proper estimate for each potential μ_i. Consider the general form of the ion reaction for metallic elements:

$$x_i M_{i,Re} + z_i H_2 O \rightleftharpoons y_i M_{i,Ox} + m_i H^+ + n_i e \tag{3}$$
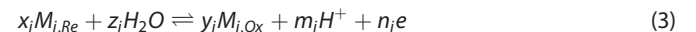
where $\{x_i, z_i, y_i, m_i, n_i\}$ are the stoichiometric coefficients for the corresponding chemical substances. The subscripts Re and Ox of M denote the reduction and oxidation states, respectively. The Nernst equation for each item of content can be constructed as:

$$\mu_i = \mu_{\Theta,i} + \frac{RT}{n_i F} \ln\left(\frac{[\alpha_{Ox}^{y_i} \alpha_{H^+}^{m_i}]}{[\alpha_{Re}^{x_i}]}\right) = \mu_{\Theta,i} + \frac{RT}{n_i F}\left[\ln\left(\frac{\alpha_{Ox}^{y_i}}{\alpha_{Re}^{x_i}}\right) + m_i \ln(\alpha_{H^+})\right] \tag{4}$$

where Θ refers to the standard state and $\alpha_{Ox}^{y_i}, \alpha_{Re}^{x_i}, \alpha_{H^+}^{m_i}$ are the activities of the corresponding oxidation state metal, reduction state metal, and hydrogen ions in the solution, respectively. In an

Table 2. Standard electrode potential (V)[39]

Redox pair	Fe^{2+}/Fe	Cr^{3+}/Cr	W^{6+}/W	Cu^{2+}/Cu
$\mu_{\Theta, i}$	−0.89	−0.74	−0.09	+0.337
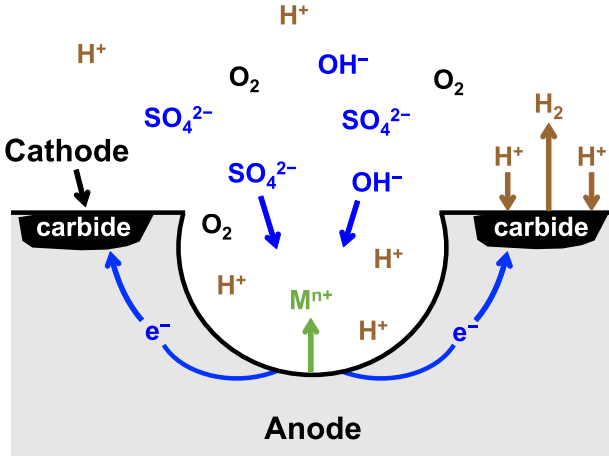
Fig. 13 Schematic diagram of micro corrosion cell model

infinite solution we assume here, $\alpha_{Ox}^{y_i}, \alpha_{Re}^{x_i} \to 0^+$. Therefore, the result of the limitation $\ln(\alpha_{Ox}^{y_i}/\alpha_{Re}^{x_i})$ has a close connection with the coefficients x_i and y_i. Considering the infimum (greatest lower bound) for our case, which corresponds physically to the worst situation in which no protective oxide is formed during corrosion, the real reaction for Eq. (3) in the anode can be simplified by the ionic formula as:

$$x_i M_{i,Re} - y_i n_i' e \rightleftharpoons y_i M_{i,Ox}^{n_i'+} \tag{5}$$

According to the principle of charge conservation, the relationship $x_i \equiv y_i$ must be established. Therefore, $\alpha_{Ox}^{y_i}$ and $\alpha_{Re}^{x_i}$ are of the same infinitesimal order, $\lim\limits_{\alpha_{Ox}^{y_i}, \alpha_{Re}^{x_i} \to 0^+} \ln(\alpha_{Ox}^{y_i}/\alpha_{Re}^{x_i}) = 0$. Equation (4) can be written as:

$$\mu_i = \mu_{\Theta,i} + \frac{RT}{n_i F}[\ln(a_{H^+}) + (m_i - 1)\ln(a_{H^+})] \tag{6}$$

Because the hydrogen evolution reaction occurs from the cathode, the potential there can be approximated by the hydrogen potential: $\widehat{\mu_C} = \mu_{\Theta,H} + [(RT)/(n_t F)]\ln(a_{H^+}) = [(RT)/(n_t F)]\ln(a_{H^+})$. According to the principle of electron conservation between an anode and a cathode, the relationship $n_t = \sum_i w_i n_i$ must be established. As a result, the difference in the potential between the cathode and anode will be established according to the following relationship:

$$\begin{aligned}
\hat{\mu} &= \widehat{\mu_C} - \widehat{\mu_{mix,A}} = \widehat{\mu_C} - \sum_i w_i \mu_i \\
&= \frac{RT}{n_t F}\ln(a_{H^+}) - \sum_i w_i\{\mu_{\Theta,i} + \frac{RT}{n_i F}[\ln(a_{H^+}) + (m_i - 1)\ln(a_{H^+})]\} \\
&= \frac{RT}{n_t F}\ln(a_{H^+}) - \sum_i w_i\mu_{\Theta,i} - \frac{RT}{F}\ln(a_{H^+})\sum_i w_i \frac{1}{n_i} - \frac{RT}{F}\ln(a_{H^+})\sum_i w_i \frac{(m_i-1)}{n_i} \\
&= -\frac{2.3RT}{n_t F}\text{pH} - \sum_i w_i\mu_{\Theta,i} + \frac{2.3RT}{F}\text{pH}\sum_i w_i \frac{1}{n_i} + \frac{2.3RT}{F}\text{pH}\sum_i w_i \frac{(m_i-1)}{n_i}
\end{aligned} \tag{7}$$

The function $f(n) = n^{-1}$ possesses convex properties when $n \in \mathbb{R}^+$. The conditions $w_i > 0$, $\forall i$, and $\sum w_i = 1$ suggest that $\boldsymbol{w}$ in Eq. (2) can be seen as a certain probability mass function p. According to Jensen's inequality, $E_p[f(\mathbf{n})] \geq f(E_p[\mathbf{n}])$; therefore, the

relationship $\sum_i w_i(1/n_i) \geq 1/(\sum_i w_i n_i) = 1/n_t$ can be obtained. As a result, the Eq. (7) will be:

$$\begin{aligned}
\hat{\mu} &= \frac{2.3RT}{F}\text{pH}\sum_i w_i \frac{(m_i-1)}{n_i} - \sum_i w_i\mu_{\Theta,i} \\
&\quad + \frac{2.3RT}{F}\text{pH}\left(\sum_i w_i \frac{1}{n_i} - \frac{1}{\sum_i w_i n_i}\right) \\
&\geq \frac{2.3RT}{F}\text{pH}\sum_i w_i \frac{(m_i-1)}{n_i} + \sum_i w_i(-\mu_{\Theta,i})
\end{aligned} \tag{8}$$

The values of $\mu_{\Theta,i}$ correspond exactly to the values in Table 2[39] for all content. The pH for the 1 N H_2SO_4 solution is approximately 0.3, while the minimum for m_i (the possible chemical valence of metals, $m_i \in \mathbb{N}^+$) is 2. n_i is also a positive integer. Thus, the first item in Eq. (8) is always positive, albeit negligibly small. As corrosion progresses, the energy of the entire system tends to decrease. Considering Table 2, it is not difficult to understand why this is so: the Cu-free sample exhibits an increasing W concentration at the surface, while Fe at the surface is consumed through an anodic reaction during corrosion. Although a fractional increase in W can decrease the difference in potential $\hat{\mu}$ to some extent, the value of $\hat{\mu}$ will invariably be positive because all $\mu_{\Theta,i}$ are negative. This was already confirmed in the dissolution tendency and the surface chemistry (Figs. 9b and 12a). Thus, there will always be a difference in potential $\hat{\mu}$ between the cathode and anode and it will never decrease to 0. Therefore, the corrosion process will never stop. In contrast, with the addition of Cu, the amount of Cu in the matrix increases (as confirmed in Figs. 10b and 13b, d) as an anodic substance during corrosion, because the standard potential for the Cu^{2+}/Cu redox pair is positive. Consequently, the difference in potential $\hat{\mu}$ for Cu addition can theoretically decrease to 0 with a fractional increase in Cu. Thus, the driving force behind the corrosion is removed and, consequently, further reactions in the Cu-added alloys are significantly inhibited.

The SEM images show that numerous secondary carbide particles formed in the martensitic matrices after both the Cu-free and Cu-added alloy systems were water-quenched. STEM observations suggest that the primary and secondary carbides possess similar structures and compositions. Hence, it is reasonable to treat them as the same substance during corrosion. Based on this inference, we find that the water quenching treatment increases the initial number of micro corrosion cells for both alloys. This will, in turn, increase the corrosion rate, as is evident in Fig. 7. The lattice defects such as grain boundaries and dislocations, introduced upon the martensitic transformation, also contribute to such severe corrosion reactions via enhanced diffusion within the matrix. However, for the Cu-added alloy, the resistance polarisation induced by the Cu concentrated on the surface of the sample is more effective at inhibiting corrosion. The corrosion rate of the Cu-added alloy is barely accelerated if only the number of micro corrosion cells is increased. This interpretation corresponds to the result obtained in the immersion tests.

The improved corrosion resistance due to Cu addition in the designed alloy relies on the gradual enrichment of Cu on the surface. The mechanism based on dealloying at the early stage of corrosion is similar to the Cu re-deposition mechanism proposed previously.[19,20] Nonetheless, the present study demonstrated that such an approach can be applied to high-carbon steels containing numerous carbide precipitates. The knowledge obtained as a result of this study and the proposed theoretical approach can be extended to other alloy systems in various corrosive environments.

METHODS

Sample preparation

Samples of the Fe–16Cr–3W–1C (mass%) alloys with and without 2 mass% Cu were fabricated using an arc melting furnace (ACM-08-1000S, DIAVAC, Japan) from elemental substances (with a purity greater than 99.9%) and

were then sliced with a fine cutter. Some of the alloy samples were sealed with Ar gas in quartz tubes and then heat-treated at 1000 °C for 2 h, followed by water quenching.

Microstructural observations

Microstructural observations for the specimens were performed using a SEM (SU3500, Hitachi, Japan) at an accelerating voltage of 15 kV. EDS was also utilised to investigate the distribution of the alloying elements. EBSD scans were performed by field-emission SEM (XL30S-FEG, FEI, USA) at 15 kV. The EBSD data were accumulated and analysed using data acquisition and analysis software (TSL-OIM 7.3, EDAX, USA). XRD measurements were performed using a PANalytical X'Pert MPD diffractometer with Cu $K\alpha$ radiation at an acceleration voltage of 45 kV and a current of 40 mA. To investigate the potential distribution of the sample surfaces, KFM measurements were conducted using a scanning probe microscope (SPM) (Multi-Mode 8, Bruker AXS, Germany). In the KFM measurements, the surface potential values were calibrated using an Au standard. The measured area was set to 20 µm × 20 µm. The specimens taken from the as-cast and quenched samples were ground using silicon carbide papers up to grade 3000. The samples were then polished with a cloth plate moistened with colloidal silica (OP-S suspension, Struers, Japan), followed by ultrasonic cleaning using acetone and distilled water.

STEM observations and EDS elemental mapping were conducted using a FEI TITAN[3] G2 60–300 S/TEM operating at 300 kV with a double spherical aberration (Cs) corrector. The sample for the STEM observations was prepared with a focused ion beam (FIB) system (Quanta 200 3D, FEI, USA).

Hardness test

The Vickers hardness of the as-cast and quenched samples was measured using a Vickers microhardness tester (HMV, Shimadzu, Japan). A force of 9.8 N was applied for an indentation duration of 10 s for each measurement. The hardness measurements were performed ten times for each specimen, after which the average values and corresponding standard deviations were calculated from these measurements. To determine the significance of the differences between the two sets of data collected, we used a paired two-sample Student's t-test. A p-value of <0.05 was considered statistically significant.

Immersion test

The PIM manufacturing of PPS was conducted at temperatures in the range of 140–300 °C. However, such experimental conditions are impractical in the laboratory and should be modified. It was reported that the corrosion rate of carbon steels can be significantly increased by decreasing the pH or increasing the temperature of the corrosion media.[40] Therefore, to simulate the corrosion behaviour at the process temperature used for PIM manufacturing, the immersion tests were conducted in a relatively concentrated H_2SO_4 solution

Immersion tests were conducted at room temperature in accordance with the NACE TM0169 standard.[41] The samples were cut to approximately $7 \times 8 \times 1.5$ mm³. A 1 N sulfuric acid solution was prepared using H_2SO_4 (Wako Pure Chemical Industries, Japan) and deionised water. The specimens were immersed in 40 ml of H_2SO_4 corrosion media placed in Teflon crucibles at an ambient temperature. The specimens that were taken out from the crucibles were cleaned with distilled water, dried, and finally measured using an electronic weighing system. This process was repeated every hour for a total of 7 h. The weight loss determined using Eq. (9) was selected to evaluate the corrosion performances of the samples, as follows:

$$\Delta m = (m_i - m_0)/A, \quad (i = 1, \ldots, 7) \qquad (9)$$

where i is the indicator for the corrosion period (hour(s)), while m_i and m_0 are the masses of the sample before and after immersion treatment. A is the surface area of the specimen determined by its dimensions before the immersion test. The corrosion rate (mg cm^{-2} h^{-1}) can also be calculated from the weight loss data if m_0 is substituted for m_{i-1} in Eq. (9) and then applied to every hour individually.

After the immersion tests, the corroded surfaces of the samples were observed by SEM (SU3500, Hitachi, Japan) at 15 kV. The surface roughness of the samples was evaluated using a 3D-measuring microscope (One-Shot 3D VR-3200, Keyence, Japan). An inductively coupled plasma optical emission spectrometer (ICP-OES, IRIS Advantage DUO, Thermo Fisher Scientific, USA) was used to evaluate the

quantities of the metallic elements in the H_2SO_4 solutions for the as-cast specimens after 7 h of immersion. The corroded surfaces of the specimens were analysed after 1 h of immersion by XPS (Axis ultra DLD, Kratos Analytical, UK) using monochromatic Al $K\alpha$ X-ray radiation (1486.7 eV). The step sizes used for the survey and narrow scans were 1 and 0.1 eV, respectively. The spectra were calibrated using the hydrocarbon peak at 284.8 eV and the chemical states of the elements were determined from the peak positions obtained by deconvoluting the high-resolution scans. The immersed specimens were cleaned with distilled water and then dried in air before analysis with XPS. The XPS-based depth profiles were acquired by etching away the surface layers using an inert Ar gas ion gun. The depth at which the samples were probed was evaluated using SiO_2 as the etch-rate reference material to convert the sputtering time into the depth.

AUTHOR CONTRIBUTIONS

K.Y. and A.C. conceived the concept of the research and designed the experiments. C.Z. and H.B. contributed to the preparation of the alloys and performed the experimental analysis. C.Z. and K.Y. wrote the manuscript. All the authors contributed to the interpretation of the experimental data, discussed the results, and commented on the manuscript.

ADDITIONAL INFORMATION

REFERENCES

1. Rahate, A. S., Nemade, K. R. & Waghuley, S. A. Polyphenylene sulfide (PPS): state of the art and applications. *Rev. Chem. Eng.* **29**, 471–489 (2013).
2. He, B. Reseach on the failure and material selection of plastic mold. *Procedia Eng.* **23**, 46–52 (2011).
3. Sugama, T. & Carciello, N. R. Corrosion protection of steel and bond durability at polyphenylene sulfide-to-anhydrous zinc phosphate interfaces. *J. Appl. Polym. Sci.* **45**, 1291–1301 (1992).
4. Kikuchi, M. Properties of stainless steel at elevated temperature. *Sanyo Tech. Rep.* **21**, 11–27 (2014).
5. Stiller, K. et al. High resolution microanalytical study of precipitation in a powder metallurgical high speed steel. *Acta Metall.* **32**, 1457–1467 (1984).
6. Simchi, A. & Asgharzadeh, H. Densification and microstructural evaluation during laser sintering of M2 high speed steel powder. *Mater. Sci. Technol.* **20**, 1462–1468 (2004).
7. Pagounis, E. & Lindroos, V. K. Processing and properties of particulate reinforced steel matrix composites. *Mate. Sci. Eng. A* **246**, 221–234 (1998).
8. Pickering, H. W. & Frankenthal, R. P. On the mechanism of localized corrosion of iron and stainless steel II. Electrochemical studies. *J. Electrochem. Soc.* **119**, 1297–1304 (1972).
9. Anantha, K. H. et al. Correlative microstructure analysis and in situ corrosion study of AISI 420 martensitic stainless steel for plastic molding applications. *J. Electrochem. Soc.* **164**, C85–C93 (2017).

10. Park, J. W., Lee, H. C. & Lee, S. Composition, microstructure, hardness, and wear properties of high-speed steel rolls. *Metall. Mater. Trans. A* **30**, 399–409 (1999).

11. Kim, C. K. et al. Effects of alloying elements on microstructure, hardness, and fracture toughness of centrifugally cast high-speed steel rolls. *Metall. Mater. Trans. A* **36**, 87–97 (2005).

12. Shtansky, D. V. & Inden, G. Phase transformation in Fe-Mo-C and Fe-W-C steels—I. The structural evolution during tempering at 700 °C. *Acta Mater.* **45**, 2861–2878 (1997).

13. Zhou, S., Dai, X. & Zheng, H. Microstructure and wear resistance of Fe-based WC coating by multi-track overlapping laser induction hybrid rapid cladding. *Opt. Laser Technol.* **44**, 190–197 (2012).

14. Andersson, J.-O., Guillermet, A. F. & Gustafson, P. On the lattice stabilities for Cr, Mo and W. *Calphad* **11**, 361–364 (1987).

15. Gustafson, P. A thermodynamic evaluation of the C-Fe-W system. *Metall. Mater. Trans. A* **18**, 175–188 (1987).

16. Gustafson, P. An experimental study and a thermodynamic evaluation of the Cr-Fe-W system. *Metall. Mater. Trans. A* **19**, 2531–2546 (1988).

17. Greene, N. D., Bishop, C. R. & Stern, M. Corrosion and electrochemical behavior of chromium-noble metal alloys. *J. Electrochem. Soc.* **108**, 836–841 (1961).

18. Itzhak, D. & Peled, P. The effect of Cu addition on the corrosion behaviour of sintered stainless steel in H_2SO_4 environment. *Corros. Sci.* **26**, 49–54 (1986).

19. Hong, J. H., Lee, S. H., Kim, J. G. & Yoon, J. B. Corrosion behaviour of copper containing low alloy steels in sulphuric acid. *Corros. Sci.* **54**, 174–182 (2012).

20. Pardo, A. et al. Influence of Cu and Sn content in the corrosion of AISI 304 and 316 stainless steels in H_2SO_4. *Corros. Sci.* **48**, 1075–1092 (2006).

21. Stawstrom, C. & Hillert, M. An improved depleted-zone theory of intergranular corrosion of 18-8 stainless steel. *J. Iron Steel Inst.* **207**, 77–85 (1969).

22. Singhal, L. K. & Martin, J. W. The nucleation and growth of widmannstätten $M_{23}C_6$ precipitation in an austenitic stainless steel. *Acta Metall.* **16**, 1159–1165 (1968).

23. Číhal, V. & Kašová, I. Relation between carbide precipitation and intercrystalline corrosion of stainless steels. *Corros. Sci.* **10**, 875–881 (1970).

24. Doğan, Ö. N. & Hawk, J. A. Effect of carbide orientation on abrasion of high Cr white cast iron. *Wear* **189**, 136–142 (1995).

25. Neville, A., Reza, F., Chiovelli, S. & Revega, T. Characterization and corrosion behavior of high-chromium white cast irons. *Metall. Mater. Trans. A* **37**, 2339–2347 (2006).

26. Hong, S. G., Lee, W. B. & Park, C. G. The effects of tungsten addition on the microstructural stability of 9Cr-Mo Steels. *J. Nucl. Mater.* **288**, 202–207 (2001).

27. Yoshizawa, M., Igarashi, M. & Nishizawa, T. Effect of tungsten on the ostwald ripening of $M_{23}C_6$ carbides in martensitic heat resistant steel. *Tetsu-To-Hagane* **91**, 272–277 (2005).

28. Ghosh, S. The role of tungsten in the coarsening behaviour of $M_{23}C_6$ carbide in 9Cr-W steels at 600 °C. *J. Mater. Sci.* **45**, 1823–1829 (2010).

29. Inoue, A., Arakawa, S. & Masumoto, T. Effect of alloying elements on defect structure and hardness of $M_{23}C_6$ type carbides. *Trans. Japan Inst. Metals* **20**, 585–592 (1979).

30. Miyamoto, G., Iwata, N., Takayama, N. & Furuhara, T. Mapping the parent austenite orientation reconstructed from the orientation of martensite by ebsd and its application to ausformed martensite. *Acta Mater.* **58**, 6393–6403 (2010).

31. Bishop, C. *Pattern Recognition and Machine Learning* (Springer, New York, 2006).

32. Yin, L. *FEM Modelling of Micro-galvanic Corrosion in Al Alloys Induced by Inter-metallic Particles: Exploration of Chemical and Geometrical Effects*. PhD thesis (KTH Royal Institute of Technology, 2018).

33. Chaker, V. *Corrosion forms and control for infrastructure*. (ASTM, Philadelphia, 1992).

34. Huang, Y. et al. *Materials Corrosion and Protection*. (De Gruyter, Berlin, 2018).

35. Perez, N et al. *Electrochemistry and Corrosion Science* (Springer, Boston, 2004).

36. Revie, R. W. & Uhlig, H. H. *Corrosion and corrosion control: An introduction to corrosion science and engineering*. (Wiley, New York, 2008).

37. Fu, J., Deng, Z. & Detsi, E. *Nanoporous Gold Formation by Free Corrosion Dealloying of Gold-Silver Alloys in Nonoxidizing Acids Driven by Catalytic Oxygen Reduction Reaction*, pages 155–166. *JOM*, **71**, 1581–1589 (2010).

38. Frigyik, B. A., Kapila, A. & Gupta, M. R. *Introduction to the Dirichlet distribution and related processes*. Dept. Elect. Eng., Univ. Washington, Seattle, WA, USA, Tech. Rep. UWEETR-2010-0006, 1–27 (2010).

39. Bard, A. J., Parsons, R. & Jordan, J. *Standard potentials in aqueous solution*. (CRC Press, Boca Raton, 1985).

40. Whitman, G. W., Russell, R. P. & Altieri, V. J. Effect of hydrogen-ion concentration on the submerged corrosion of steel. *Ind. Eng. Chem.* **16**, 665–670 (1924).

41. NACE TM0169. *Laboratory corrosion testing of metals*. (NACE International, Houston, 2012).